Exploring Alzheimer's disease mouse brain through X-ray phase contrast tomography: From the cell to the organ

Lorenzo Massimi [a], Inna Bukreeva [a,b], Giulia Santamaria [c], Michela Fratini [a,d], Alessandro Corbelli [c], Francesco Brun [a], Stefano Fumagalli [c], Laura Maugeri [a,d], Alexandra Pacureanu [e], Peter Cloetens [e], Nicola Pieroni [a], Fabio Fiordaliso [c], Gianluigi Forloni [c], Antonio Uccelli [f,g], Nicole Kerlero de Rosbo [f], Claudia Balducci [c,*,1], Alessia Cedola [a,b,**,1]

[a] *Istituto di Nanotecnologia, Consiglio Nazionale delle Ricerche, Rome, Italy*
[b] *Dipartimento di Fisica, Università Sapienza, Rome, Italy*
[c] *Istituto di Ricerche Farmacologiche Mario Negri IRCCS, Milan, Italy*
[d] *IRCCS Fondazione Santa Lucia, Rome, Italy*
[e] *European Synchrotron Radiation Facility, Grenoble, France*
[f] *DINOGMI, Università degli Studi di Genova, Genoa, Italy*
[g] *Ospedale Policlinico San Martino, Genoa, Italy*

ARTICLE INFO

Keywords:
Alzheimer disease neuropathology
Beta-amyloid plaques
Animal model
X-ray phase contrast tomography
Synchrotron radiation

ABSTRACT

Alzheimer's disease (AD), the most common form of dementia, is a progressive neurodegenerative disorder associated with aberrant production of beta-amyloid (Aβ) peptide depositing in brain as amyloid plaques. While animal models allow investigation of disease progression and therapeutic efficacy, technology to fully dissect the pathological mechanisms of this complex disease at cellular and vascular levels is lacking.

X-ray phase contrast tomography (XPCT) is an advanced non-destructive 3D multi-scale direct imaging from the cell through to the whole brain, with exceptional spatial and contrast resolution. We exploit XPCT to simultaneously analyse disease-relevant vascular and neuronal networks in AD mouse brain, without sectioning and staining. The findings clearly show the different typologies and internal structures of Aβ plaques, together with their interaction with patho/physiological cellular and neuro-vascular microenvironment. XPCT enables for the first time a detailed visualization of amyloid-angiopathy at capillary level, which is impossible to achieve with other approaches.

XPCT emerges as added-value technology to explore AD mouse brain as a whole, preserving tissue chemistry and structure, enabling the comparison of physiological vs. pathological states at the level of crucial disease targets. In-vivo translation will permit to monitor emerging therapeutic approaches and possibly shed new light on pathological mechanisms of neurodegenerative diseases.

1. Introduction

The use of animal models to mimic neurodegenerative disorders allows the investigation of neuropathogenic mechanisms and the monitoring of disease progression and therapeutic efficacy (Balducci and Forloni, 2011). This is particularly important for research on Alzheimer's disease (AD), based on the complexity of its neuropathology involving synaptic and cognitive dysfunction, neuroinflammation, brain angiopathy, neuronal cell death, and gross brain atrophy (Selkoe, 2011). The causes and progression of AD are not well understood as yet. The main histopathological brain lesions of AD patients are represented by extracellular senile plaques composed of Aβ aggregates, and by intracellular neurofibrillary tangles enriched in hyperphosphorylated *tau* protein.

One of the unmet needs common to neurodegenerative diseases of the CNS, including AD, is the possibility to investigate crucial

* Corresponding author. Istituto di Ricerche Farmacologiche Mario Negri IRCCS, Milan, Italy.
** Corresponding author. Istituto di Nanotecnologia, Consiglio Nazionale delle Ricerche, Rome, Italy.
E-mail addresses: claudia.balducci@marionegri.it (C. Balducci), alessia.cedola@cnr.it (A. Cedola).
[1] equal contributions.

neuropathological signatures and therapeutic efficacy at the fine level. Ideally, this would require direct imaging of the whole brain in a 3D fashion, rather than of isolated slices of brain tissue having undergone blood removal, freezing at extremely low temperature, and manipulation with aggressive fixatives and various detergents. Direct 3D-imaging would allow simultaneous analyses of (i) brain alterations in various cell populations (neuronal loss, gliosis, peripheral infiltrates); (ii) structural changes in terms of cell density and organization (brain atrophy); (iii) modifications in vascular networks and integrity (cerebral amyloid angiopathy).

The ambitious possibility to achieve a 3D-imaging of the highly complex neuronal and vascular networks communicating with disease-relevant cells, while preserving tissue chemistry, is not possible with conventional indirect immunohistochemical techniques, as these necessitate chemical tissue manipulation to add fluorescence/chromogenic reporters. Magnetic resonance imaging help circumvent these problems, but remains limited by spatial resolution of a few mm (Dona et al., 2016). In contrast, X-ray tomography overcomes spatial resolution limits; however, it fails to image soft tissues. Such a lack can be filled by X-ray phase contrast tomography (XPCT), which makes possible multi-scale 3D biomedical imaging of neuronal and vascular networks ranging from cells through to brain as a whole (Bukreeva et al., 2017; Cedola et al., 2017; Fratini et al., 2015). XPCT is particularly useful for low-absorbing bio-medical samples, with a gain in contrast resolution reaching up to 1000 folds that of conventional tomography. XPCT, with its high resolution and large field of view, is rapidly gaining importance in the investigation of neurodegenerative diseases, such as AD and multiple sclerosis (Pinzer et al., 2012).

2. Materials and methods

2.1. Animals

APPswe/PS1dE9 (APP/PS1) transgenic male mice [B6C3-Tg(APPswe, PSEN1dE9)85Dbo/Mmjax mice] and age-matched WT littermates were purchased from Jackson Laboratories (USA). All procedures involving animals and their care were conducted according to European Union (EEC Council Directive 86/609, OJ L 358,1; 12 December 1987) and Italian (D.L. n.116, G.U. suppl. 40, 18 February 1992) laws and policies. They were reviewed and approved by the Mario Negri Institute Animal Care and Use Committee.

2.2. Preparation of the samples for XPCT and nano-XPCT

The preparation of the samples for ex-vivo XPCT is necessary to ensure the integrity of the tissue that would otherwise degrade. However, as widely shown, it preserves the structure and chemistry of the tissues. Nano-XPCT requires a sample preparation similar to that used for SEM experiments, but tissue chemistry is still preserved.

XPCT: Mice were killed under CO_2 to drastically reduce bleeding. Brains were removed, placed in paraformaldehyde for 24 h, and stored in 70% EtOH at 4 °C until analysis. Prior to XPCT analysis, the samples were included in agar agar, which keeps them hydrated and prevent both radiation damage and movement of the samples during the measurement.

Nano-XPCT: Hippocampus were dissected out and placed in 2.5% gluteraldehyde in 0.1 M cacodylate buffer, pH 7.2, for 3 h at room temperature. Samples were post-fixed in osmium tetroxide (1% in 0.1 M cacodylate buffer, pH 7.2; 1 h) and uranyl acetate (1% in water; 1 h), dehydrated through a graded ethanol series (70/95/100%), put in propylene oxide, and embedded in epoxy resin (Sigma-Aldrich, St. Louis, MO 63103 USA) at 42 °C overnight and for 2 days at 60 °C.

2.3. Experimental XPCT and nano-XPCT set-ups

i) The XPCT experiment used monochromatic incident X-ray energy at 17 keV. The sample-detector distance was set at 5 cm. The detector has an effective pixel size of 1.625 μm. The tomography was produced by means of 3000 projections covering a total angle range of 360°. The acquisition time for each angular position was 50 ms. The total brain volume was acquired in about 15 min. We exploited the half-acquisition mode, which pertains specifically the acquisition of sample horizontally larger than the field of view (FOV) of the camera. In this acquisition mode the sample is positioned outside the rotation center of the stage so that half of the sample is outside the FOV. We acquired over an angular range of 360°. The projections acquired during the first 180° will provide information on the first part of the sample, while the projections acquired from 180 to 360° will provide information on the sample region which was initially out of the FOV.

Data pre-processing, phase retrieval and reconstruction were performed with SYRMEP Tomo Project software (Brun et al., 2017; Massimi et al., 2018) and optimized scripts. Image analysis was performed using ImageJ and the 3D rendering images were obtained using VG studio Max software.

ii) The nano-XPCT experiments were carried out at Nano-Imaging ID16A beamline of the ESRF. A pair of multilayer coated Kirkpatrick-Baez optics was used to focus the X-rays (~30 nm) at 17 keV. The sample is put in the divergent beam downstream of the focus to produce magnified phase contrast images. The projection geometry also allows zooming into specific regions of a large sample by combining scans with different magnifications and fields of view (Bartels et al., 2015; Mokso and Cloetens, 2007). By measuring the Fresnel diffraction patterns at different effective propagation distances, the phase maps of the sample can be retrieved via holographic reconstruction, this so-called phase retrieval procedure (Cloetens et al., 1999) being implemented using GNU Octave software. Magnified radiographs were recorded onto an X-ray detector using a FReLoN charged-coupled device. For one tomography scan, 1500 projections were acquired with 0.32 s exposure time and 50 nm effective pixel size. Tomography scans at four different foci to sample distances were acquired to complete one holotomography scan. The tomographic reconstruction was obtained with ESRF PyHST software package.

2.4. Transmission electron microscopy

Samples were prepared as for nano-XPCT and ultrathin sections (50 nm) were cut with a Leica EM UC6 ultramicrotome (Leica Microsystems, Vienna, Austria), counterstained with lead citrate (0.004% in water) and examined with an energy filter transmission electron microscope (EFTEM Libra120, Carl Zeiss NTS GmbH, Oberkochen, Germany).

2.5. Immunofluorescence for astrocytes, axons, and amyloid plaques

APP/PS1 coronal brain cryostat sections were collected in 100 mM PBS for immunofluorescence analysis of astrocytes, and axons, and double-stained for amyloid plaques. Freely-floating brain slices were incubated overnight at 4 °C with the primary antibodies against MAP2 (1:2000, Abcam; 24 h, 4 °C) for axons; GFAP (1:3500; Chemicon Int. Inc., Temecula, USA) for astrocytes, followed by incubation with the appropriate secondary antibodies conjugated with either Alexa 546 or Alexa 695 (1:500, Molecular Probes). Plaques were revealed by exposure of the slices to the fluorescent dye X34.

2.6. Structured illumination microscopy (SIM)

SIM analysis of brain sections was performed on a Nikon SIM system. Tissues were imaged at laser excitation of 405 (for X34), 561 (for MAP-2) and 640 (for GFAP) nm with a 3D-SIM acquisition protocol. Sixteen-bit images sized 1024 × 1024 pixels with a single pixel of 0.030 μm were acquired in a grey-level range of 0–16000 to exploit the linear range of the camera (iXon ultra DU-897U, Andor) and to avoid saturation. Three-

dimensional Z-stacks were scanned with a 0.125 µm step size over 2–3 µm. Raw and reconstructed images were validated with the SIM-check plugin of ImageJ (Ball et al., 2015) to rule out image artifacts (Demmerle et al., 2017; Culley et al., 2018).

Only those meeting validation criteria as shown in Fig. S1 were included in the study. Images were finally managed with GIMP (Gnu Image Manipulation Program).

3. Results

Here, we present an extensive multi-scale investigation of the AD mouse brain imaged with XPCT, providing the 3D structure of the hippocampus at micro and nano scale and the description of the internal structure of amyloid plaques, capillaries, and of their interaction with the surrounding brain microenvironment, including neurons and glial cells. We used the APP/PS1 mouse AD model. These mice carry a Swedish human mutation in the amyloid precursor protein (APP) gene and a deletion of exon 9 on the presenilin 1 (PS1) gene (Jankowsky et al., 2001). APP/PS1 mice are the AD model most widely used and best characterized by us and others (Balducci et al., 2014; Gregori et al., 2017; Mancini et al., 2017), with Aβ plaques starting to be detectable around the age of 6–8 months (Holcomb et al., 1998), accompanied by intense inflammation, atrophy, and vascular damage in brain.

Two XPCT experiments in free-space propagation mode (Bravin et al., 2013) were performed with respective spatial resolutions of 1.625 µm (voxel side) at Tomcat-SLS in Villigen, Switzerland, and 50 nm (equal in the three directions) at ID16A-ESRF in Grenoble, France, used previously for nano-3D neuro-imaging of spinal cord of mice affected with experimental multiple sclerosis (Cedola et al., 2017), and of brain tissue of naïve mice (Khimchenko et al., 2016). In the first experiment, we obtained 3D imaging of the whole brain down to plaques and cells. In the second experiment, we explored the internal structure of the amyloid plaques and capillaries, and described their interaction with the surrounding brain microenvironment. We present the data obtained on a wild-type (WT) mouse and an APP/PS1 mouse.

Fig. 1 demonstrates that XPCT has the potentiality to dissect AD brain from the whole organ to the fine neuropathology. Thus, a virtually selected 450-µm-thick portion of whole brain is shown in Fig. 1a, while Fig. 1b–c shows a portion of the hippocampal region.

We easily distinguish both absence (Fig. 1b) and presence (Fig. 1c) of Aβ plaques in WT and APP/PS1 mouse hippocampus, respectively. The insets of Fig. 1c show single Aβ plaques in details, which are clearly different in structure. We could classify plaques as two different kinds, neuritic plaques with a dense core and neuritic plaques without a core. In the classification of plaques, the term “neuritic plaques” originates from the typical presence of dystrophic neuronal processes (dystrophic neurites) in the plaque corona surrounding the central dense nucleation core, and differences in plaque features are normally attributable to a different stage of plaque development (Duyckaerts et al., 2009; Perl, 2010).

Through nano-XPCT, with a spatial resolution of 50 nm, we imaged inside the plaques. It should be noted that in the nano-tomography images presented, the grey levels are inversely proportional to the density, with black corresponding to high-density structures, whereas white corresponds to low-density structures.

As observed in Fig. 1d, we could detect a typical neuritic plaque with a central nucleation core (Han et al., 1995); as demonstrated through transmission electron microscopy (EM), these cores are enriched in Aβ fibrils (Fig. 1e). We could also detect a different type of neuritic plaque without a central core (Fig. 1f). Both plaques were surrounded by dystrophic neurites (red arrows), widely described in both AD mouse (Blanchard et al., 2003) and patient brains (Su et al., 1993). Again, EM confirmed this pathological detail evidenced by nano-XPCT (Fig. 1g). Fig. 1 panels h and i show a 3D rendering of several deposited Aβ plaques and of a single Aβ plaque, respectively, as obtained from nano-XPCT.

XPCT is also unique in permitting a very detailed analysis of the whole brain vasculature. In particular, Fig. 2a–d shows different

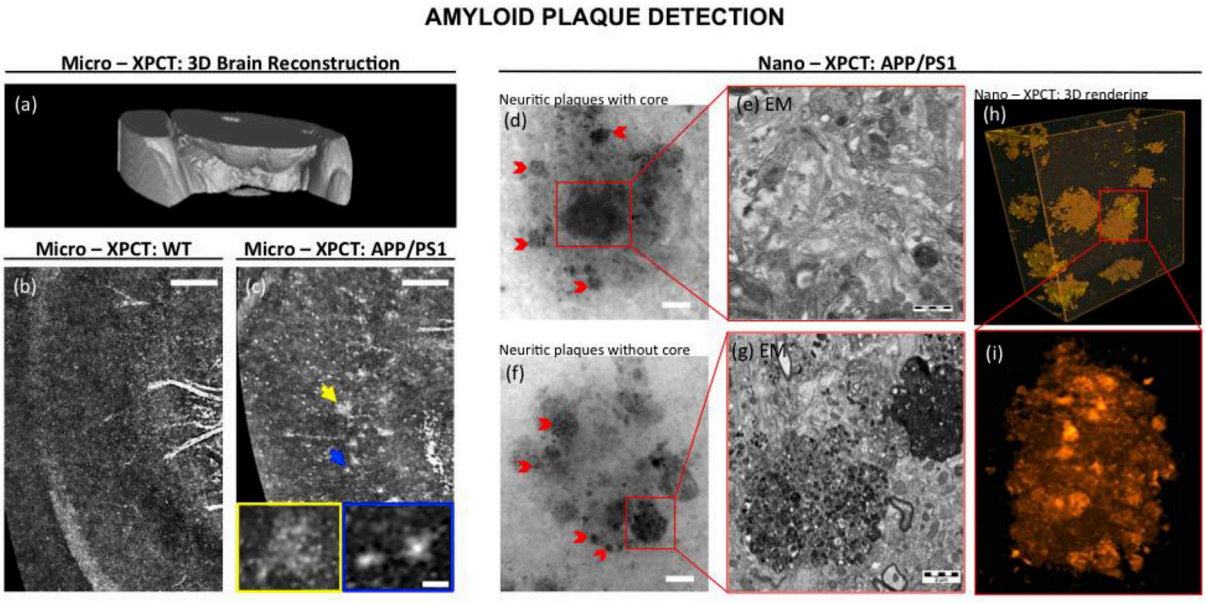

Fig. 1. XPCT allows a deep investigation of Aβ plaques. a) 3D XPCT-rendering of the virtually selected portion of mouse brain. Micro-XPCT images showing **b)** absence of plaques and **c)** clearly detectable Aβ plaques in hippocampus of WT and APP/PS1 mice, respectively. (Scale bar = 200 µm). Magnified insets in (**c**) show both neuritic cored and non-cored plaques indicated with blue and yellow arrows respectively in the smaller magnification image. (Scale bar = 30 µm). **d)** Nano-XPCT image (scale bar = 5 µm) of a cored neuritic plaque, with EM photograph (**e**) showing Aβ fibrils inside plaque cores (scale bar = 500 nm). **f)** Nano-XPCT image (scale bar = 5 µm) of a non-cored neuritic plaque enriched in dystrophic neurites inthe plaque corona. Red arrows in both **d** and **f** indicate dystrophic neurites. **g)** EM photograph confirming the presence of dystrophic neurites around plaques (scale bar = 500 nm). **h)** 3D rendering of deposited Aβ plaques and **i)** of a single Aβ plaque. Grey levels are proportional to tissue density as follows: in XPCT images (b, c), high-density structures appear white, whereas low-density structures appear black; in nano-XPCT (d, f), the grey levels are inverted.

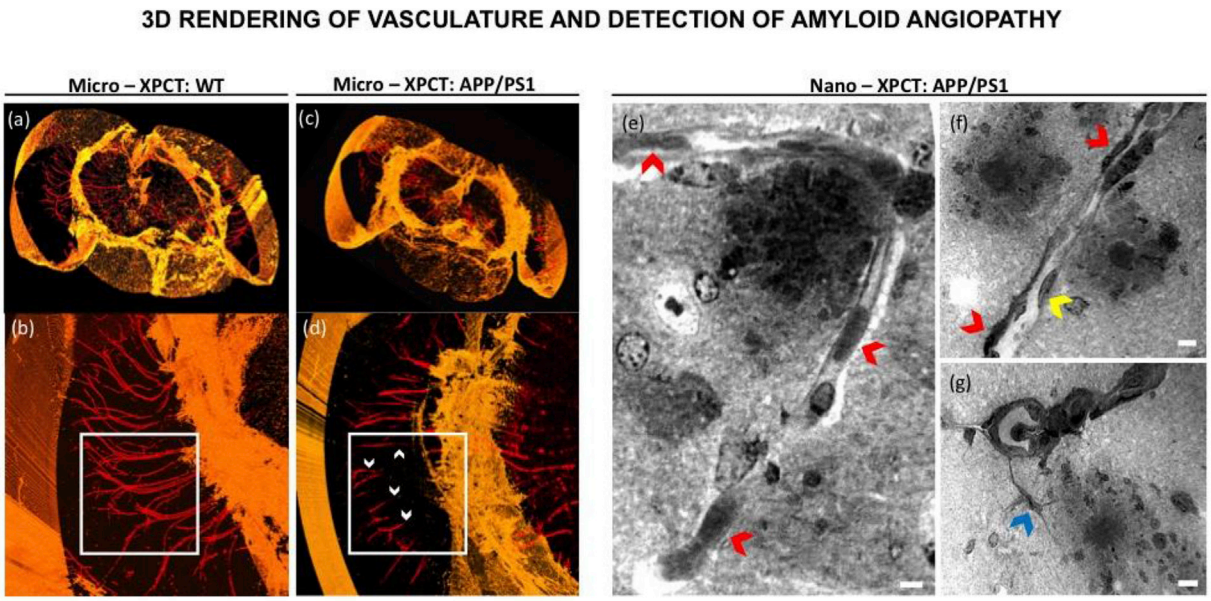

Fig. 2. XPCT shows vascular alterations in AD mouse brain. a-d) Micro–XPCT 3D-renderings of (**a-b**) normal blood vasculature in WT mouse brain, and (**c-d**) evidence of vessel loss (**d**, white frame) and interruptions (**d**, white arrows) in APP/PS1 mouse brain. **e-f)** Nano-XPCT images of brain capillaries of APP/PS1 mouse brain showing the presence of Aβ deposits inside the lumen (scale bar = 5 μm), which completely occlude the vessels (red arrows in (**e**)), or on vessel walls leading to a clear reduction in lumen volume (red arrows in (**f**)). The yellow arrow in (f) indicates an endothelial cell at the wall of the capillary. Plaques are also well distinguishable in close proximity to vessels. **g)** Nano-XPCT image showing an apparent interaction between a deposited plaque and a capillary through astrocyte end-feet (blue arrow).

enlargements of 3D renderings of the blood vessel network of the whole hippocampus, in 23-month-old WT and APP/PS1 mice, respectively, providing information on the status of the brain vasculature in terms of vessel integrity and distribution. It is worthwhile to remark that only a 3D imaging of thick sample volume allows to follow the trajectory of the vessels and thereby permitting this kind of investigation. The comparison of WT (Fig. 2a and b) and APP/PS1 (Fig. 2c and d) mice provides information on the presence of eventual vascular alterations related to AD.

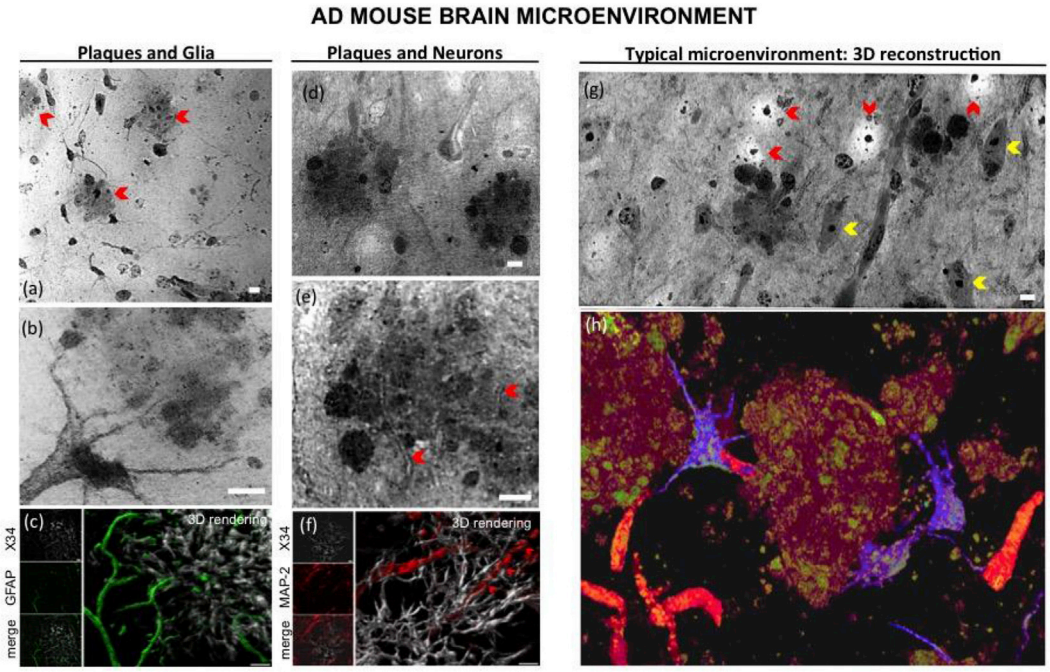

Fig. 3. Nano-XPCT describes AD mouse brain microenvironment. a) Nano-XPCT image (scale bar = 5 μm) showing hippocampal microenvironment enriched in deposited Aβ plaques and widely populated by astrocytes. **b)** Zoom of a single astrocyte whose processes surround the plaque (scale bar = 5 μm). **c)** Super-resolution immunofluorescence images (scale bar = 2 μm) of APP/PS1 brain slices stained for plaques and astrocytes, to show an astrocyte surrounding the plaque. **d-e)** Nano-XPCT images where neuronal axons are well visible across and near plaques (red arrows) (scale bar = 5 μm). **f)** Immunofluorescence images of a mouse brain slice stained for plaques and axons. **g)** Nano-XPCT image shows the clear presence of both healthy (yellow arrows) and suffering (red arrows) neurons. **h)** 3D-rendering of the microenvironment in APP/PS1 mouse brain. Violet: astrocytes; red: capillaries; brown: plaques; green: dystrophic neurites.

In the WT mouse, micro-vessels appear normally branched and distributed throughout the brain parenchyma, displaying no signs of vessel wall breakages, as can be seen in a detail shown in Fig. 2b (white frame). In contrast, Fig. 2c and d provides details on vessel status in the brain of a 23-month-old APP/PS1 mouse, with an apparent reduction in blood vessels detected in the same area (white frame). As indicated by the white arrows, some of the remaining vessels appear damaged with evident wall interruptions, as already described through XPCT in experimental multiple sclerosis (Cedola et al., 2017).

Through nano-XPCT, we collected further neuropathological details at the capillary level (Fig. 2 e-g). This enabled the exploration of the intra-capillary lumen (Fig. 2e), including the visualization of endothelial cells at the walls of the capillary (yellow arrow in Fig. 2f), and revealed the presence of Aβ deposits inside the capillary lumen (red arrows in Fig. 2e) and at the vessel walls (red arrows in Fig. 2f). Abnormality of vessel walls is considered as the main cause of brain hypo-perfusion in AD (Allen et al., 2014); XPCT provides additional information on angiopathy, particularly at capillary level, which cannot be obtained with standard techniques.

Nano-XPCT also enabled imaging of the typical 'glial barrier', which consists of astroglial end-feet surrounding the BBB and covering the majority of the parenchymal vasculature (Yamazaki and Kanekiyo, 2017). Of note is the recent demonstration of the so-called *glymphatic system*, a macroscopic waste clearance system of the neurovascular unit which utilizes a unique system of perivascular tunnels, made of astroglial cells which regulate a continuous interchange between CSF and interstitial fluid. This system apparently promotes efficient elimination of soluble proteins and metabolites from the CNS including Aβ (Jessen et al., 2015). Interestingly in this context, Fig. 2g shows an astrocyte (blue arrow in Fig. 2g) interconnecting a neuritic plaque with an apparently damaged capillary.

Nano-XPCT also permitted a detailed imaging of the microenvironment encountered around neuritic plaques and typifying an AD brain and its cellular complexity (Fig. 3). Thanks to the depth information, provided by 3D imaging and which cannot be obtained via 2D imaging, the distribution in space of the tissue components can be visualized.

In particular, Fig. 3a shows three neuritic plaques (red arrows) surrounded by astrocytes. Fig. 3b shows a zoom of astrocyte-plaque contact in a different zone of the same sample. Astrocytes in the periphery of the corona of plaques are widely described in the literature (Duyckaerts et al., 2009), and our nano-XPCT observation is supported by our immunofluorescence analysis of Aβ plaques (Fig. 3c) and astrocytes. In 3D reconstruction, images acquired in super resolution optical microscopy clearly show an astrocyte surrounding the plaque (Fig. 3c), confirming the reliability of nano-XPCT.

Thin filaments (1–3 μm in diameter), compatible with myelinated axons, were also detectable (Fig. 3d), some of which pass across the plaques, as can be seen in Fig. 3e (red arrows). Super-resolution immunofluorescence imaging, which demonstrated that these filaments were positive for MAP-2 (Fig. 3f), a marker for axons, support the description of the microstructures observed through XPCT.

In addition to its ability to image simultaneously Aβ plaques, astrocytes, and vessels, nano-XPCT permitted to investigate neuronal cells at distance or in close proximity to plaques.

Notably, we could detect the coexistence of both healthy and suffering neurons in the same zone. Thus, Fig. 3g shows normally shaped neurons (yellow arrows) with a typical dense cytoplasm (rendered as grey), indicative of pathology-spared neurons, and neurons smaller in size, with a whiter cytoplasm and a very small nucleus (red arrows) such as typically encountered in neuronal degeneration (Kuljis et al., 1997).

Fig. 3h is a 3D rendering that summarizes the potential of nano-XPCT in describing a typical microenvironment encountered in an AD mouse brain populated by plaques, where astrocytes are marked in violet, capillaries in red, and plaques in brown.

4. Conclusions

We herein demonstrate that XPCT holds the great advantage of allowing a 3D detailed investigation of the brain microenvironment in its real complexity. It permitted the reliable description of the neuropathological context encountered in different brain areas of an AD mouse model mimicking the human pathology where neuronal and vascular networks are compromised. XPCT allowed us not only to evidence the main pathological lesions of AD, such as deposited extracellular senile plaques and the presence of dystrophic neurites populating plaque corona, but also to distinguish different typologies of plaques. We could detect the presence of astrocytic processes around plaques, such as occurs in the brain of AD patients (Duyckaerts et al., 2009), and connections between plaques and capillaries through astrocytic end-feet. At vascular level, we observed capillaries featuring deposits which reduced the vessel lumen, and are likely attributable to the presence of deposited Aβ. As widely described also in the literature, we observed the presence of suffering neurons close to plaques, and healthy neurons at a certain distance from them (Mucke and Selkoe, 2012).

The possibility to faithfully image brain conditions in a 3-dimension and in such an exhaustive manner, without tissue manipulation, is a unique opportunity to dissect the neuropathology down to nano-sized details, thereby gaining a more comprehensive understanding of it. Most importantly, through XPCT we will be able to evaluate the efficacy of new therapeutic approaches in experimental models at the level of the multiple crucial neuropathological targets of AD and other neurodegenerative diseases.

Acknowledgements

This study was supported in part by the European project VOXEL "Volumetric Medical X-Ray Imaging at extremely low dose" (HORIZON 2020-Fet Open; Project reference: 665207) to A. C., the Paul Allen Foundation grant No. 12069 to C. B.. M.F. and L.M. also acknowledge the Italian Ministry of Health under the Young Researcher Grant 2013(GR-2013-02358177) for the financial support. We thank the Tomcat beamline staff for providing beam time.

Appendix A. Supplementary data

Supplementary data to this article can be found online at https://doi.org/10.1016/j.neuroimage.2018.09.044.

References

Allen, N., Robinson, A.C., Snowden, J., Davidson, Y.S., Mann, D.M.A., 2014. Patterns of cerebral amyloid angiopathy define histopathological phenotypes in Alzheimer's disease. Neuropathol. Appl. Neurobiol. 40, 136–148. https://doi.org/10.1111/nan.12070.

Balducci, C., Forloni, G., 2011. APP transgenic mice: their use and limitations. NeuroMolecular Med. 13, 117–137. https://doi.org/10.1007/s12017-010-8141-7.

Balducci, C., Mancini, S., Minniti, S., La Vitola, P., Zotti, M., Sancini, G., Mauri, M., Cagnotto, A., Colombo, L., Fiordaliso, F., Grigoli, E., Salmona, M., Snellman, A., Haaparanta-Solin, M., Forloni, G., Masserini, M., Re, F., 2014. Multifunctional liposomes reduce brain beta-amyloid burden and ameliorate memory impairment in Alzheimer's disease mouse models. J. Neurosci. 34, 14022–14031. https://doi.org/10.1523/JNEUROSCI.0284-14.2014.

Ball, G., Demmerle, J., Kaufmann, R., Davis, I., Dobbie, I.M., Schermelleh, L., 2015. SIMcheck: a toolbox for successful super-resolution structured illumination microscopy. Sci. Rep. 5, 15915. https://doi.org/10.1038/srep15915.

Bartels, M., Krenkel, M., Cloetens, P., Möbius, W., Salditt, T., 2015. Myelinated mouse nerves studied by X-ray phase contrast zoom tomography. J. Struct. Biol. 192, 561–568. https://doi.org/10.1016/j.jsb.2015.11.001.

Blanchard, V., Moussaoui, S., Czech, C., Touchet, N., Bonici, B., Planche, M., Canton, T., Jedidi, I., Gohin, M., Wirths, O., Bayer, T.A., Langui, D., Duyckaerts, C., Tremp, G., Pradier, L., 2003. Time sequence of maturation of dystrophic neurites associated with Abeta deposits in APP/PS1 transgenic mice. Exp. Neurol. 184, 247–263.

Bravin, A., Coan, P., Suortti, P., 2013. X-ray phase-contrast imaging: from pre-clinical applications towards clinics. Phys. Med. Biol. 58, R1–R35. https://doi.org/10.1088/0031-9155/58/1/R1.

Brun, F., Massimi, L., Fratini, M., Dreossi, D., Billé, F., Accardo, A., Pugliese, R., Cedola, A., 2017. SYRMEP Tomo Project: a graphical user interface for customizing

CT reconstruction workflows. Adv. Struct. Chem. Imaging 3, 4. https://doi.org/10.1186/s40679-016-0036-8.
Bukreeva, I., Campi, G., Fratini, M., Spanò, R., Bucci, D., Battaglia, G., Giove, F., Bravin, A., Uccelli, A., Venturi, C., Mastrogiacomo, M., Cedola, A., 2017. Quantitative 3D investigation of Neuronal network in mouse spinal cord model. Sci. Rep. 7, 41054. https://doi.org/10.1038/srep41054.
Cedola, A., Bravin, A., Bukreeva, I., Fratini, M., Pacureanu, A., Mittone, A., Massimi, L., Cloetens, P., Coan, P., Campi, G., Spanò, R., Brun, F., Grigoryev, V., Petrosino, V., Venturi, C., Mastrogiacomo, M., Kerlero de Rosbo, N., Uccelli, A., 2017. X-ray phase contrast tomography reveals early vascular alterations and neuronal loss in a multiple sclerosis model. Sci. Rep. 7, 5890. https://doi.org/10.1038/s41598-017-06251-7.
Cloetens, P., Ludwig, W., Baruchel, J., 1999. Holotomography: quantitative phase tomography with micrometer resolution using hard synchrotron radiation x rays. Appl. Phys. Lett. 1999 (75), 2912.
Culley, S., Albrecht, D., Jacobs, C., Pereira, P., Leterrier, C., Mercer, J., Henriques, R., 2018. Quantitative mapping and minimization of super-resolution optical imaging artifacts. Nat. Methods 15, 263–266. https://doi.org/10.1038/nmeth.4605.
Demmerle, J., Innocent, C., North, A.J., Ball, G., Müller, M., Miron, E., Matsuda, A., Dobbie, I.M., Markaki, Y., Schermelleh, L., 2017. Strategic and practical guidelines for successful structured illumination microscopy. Nat. Protoc. 12, 988–1010. https://doi.org/10.1038/nprot.2017.019.
Dona, O., Thompson, J., Druchok, C., 2016. Comprehensive review on magnetic resonance imaging in Alzheimer's disease. Crit. Rev. Biomed. Eng. 44, 213–225. https://doi.org/10.1615/CritRevBiomedEng.2016019544.
Duyckaerts, C., Delatour, B., Potier, M.C., 2009. Classification and basic pathology of Alzheimer disease. Acta Neuropathol. 118, 5–36. https://doi.org/10.1007/s00401-009-0532-1.
Fratini, M., Bukreeva, I., Campi, G., Brun, F., Tromba, G., Modregger, P., Bucci, D., Battaglia, G., Spanò, R., Mastrogiacomo, M., Requardt, H., Giove, F., Bravin, A., Cedola, A., 2015. Simultaneous submicrometric 3D imaging of the micro-vascular network and the neuronal system in a mouse spinal cord. Sci. Rep. 5, 8514. https://doi.org/10.1038/srep08514.
Gregori, M., Taylor, M., Salvati, E., Re, F., Mancini, S., Balducci, C., Forloni, G., Zambelli, V., Sesana, S., Michael, M., Michail, C., Tinker-Mill, C., Kolosov, O., Scherer, M., Harris, S., Fullwood, N.J., Masserini, M., Allsop, D., 2017 Feb. Retro-inverso peptide inhibitor nanoparticles as potent inhibitors of aggregation of the Alzheimer's Aβ peptide. Nanomedicine 13 (2), 723–732. https://doi.org/10.1016/j.nano.2016.10.006.
Han, H., Weinreb, P.H., Lansbury, P.T., 1995. The core Alzheimer's peptide NAC forms amyloid fibrils which seed and are seeded by beta-amyloid: is NAC a common trigger or target in neurodegenerative disease? Chem. Biol. 2, 163–169.
Holcomb, L., Gordon, M.N., McGowan, E., Yu, X., Benkovic, S., Jantzen, P., Wright, K., Saad, I., Mueller, R., Morgan, D., Sanders, S., Zehr, C., O'Campo, K., Hardy, J., Prada, C.M., Eckman, C., Younkin, S., Hsiao, K., Duff, K., 1998. Accelerated Alzheimer-type phenotype in transgenic mice carrying both mutant amyloid precursor protein and presenilin 1 transgenes. Nat. Med. 4, 97–100.
Jankowsky, J.L., Slunt, H.H., Ratovitski, T., Jenkins, N.A., Copeland, N.G., Borchelt, D.R., 2001. Co-expression of multiple transgenes in mouse CNS: a comparison of strategies. Biomol. Eng. 17, 157–165 [pii]. https://doi.org/S1389034401000673.
Jessen, N.A., Munk, A.S.F., Lundgaard, I., Nedergaard, M., 2015. The glymphatic system: a beginner's guide. Neurochem. Res. 40, 2583–2599. https://doi.org/10.1007/s11064-015-1581-6.
Khimchenko, A., Deyhle, H., Schulz, G., Schweighauser, G., Hench, J., Chicherova, N., Bikis, C., Hieber, S.E., Müller, B., 2016. Extending two-dimensional histology into the third dimension through conventional micro computed tomography. Neuroimage 139, 26–36. https://doi.org/10.1016/j.neuroimage.2016.06.005.
Kuljis, R.O., Xu, Y., Aguila, M.C., Baltimore, D., 1997. Degeneration of neurons, synapses, and neuropil and glial activation in a murine Atm knockout model of ataxia-telangiectasia. Proc. Natl. Acad. Sci. U.S.A. 94, 12688–12693.
Mancini, S., Balducci, C., Micotti, E., Tolomeo, D., Forloni, G., Masserini, M., Re, F., 2017 Jul 28. Multifunctional liposomes delay phenotype progression and prevent memory impairment in a presymptomatic stage mouse model of Alzheimer disease. J. Control. Release 258, 121–129. https://doi.org/10.1016/j.jconrel.2017.05.013.
Massimi, L., Brun, F., Fratini, M., Bukreeva, I., Cedola, A., 2018. An improved ring removal procedure for in-line x-ray phase contrast tomography. Phys. Med. Biol. 2018 (63), 045007.
Mokso, R., Cloetens, P., 2007. Nanoscale zoom tomography with hard x rays using Kirkpatrick-Baez optics. Appl. Phys. Lett. 90, 144104.
Mucke, L., Selkoe, D.J., 2012. Neurotoxicity of amyloid beta-protein: synaptic and network dysfunction. Cold Spring Harb Perspect Med 2, a006338. https://doi.org/10.1101/cshperspect.a006338.
Perl, D.P., 2010. Neuropathology of Alzheimer's disease. Mt. Sinai J. Med. N. Y. 77, 32–42. https://doi.org/10.1002/msj.20157.
Pinzer, B.R., Cacquevel, M., Modregger, P., McDonald, S.A., Bensadoun, J.C., Thuering, T., Aebischer, P., Stampanoni, M., 2012. Imaging brain amyloid deposition using grating-based differential phase contrast tomography. Neuroimage 61, 1336–1346. https://doi.org/10.1016/j.neuroimage.2012.03.029.
Selkoe, D.J., 2011. Alzheimer's disease. Cold Spring Harb Perspect Biol 3. https://doi.org/10.1101/cshperspect.a004457.
Su, J.H., Cummings, B.J., Cotman, C.W., 1993. Identification and distribution of axonal dystrophic neurites in Alzheimer's disease. Brain Res. 625, 228–237.
Yamazaki, Y., Kanekiyo, T., 2017. Blood-brain barrier dysfunction and the pathogenesis of Alzheimer's disease. Int. J. Mol. Sci. 18. https://doi.org/10.3390/ijms18091965.